J Mater Sci (2009) 44:6617–6628
DOI 10.1007/s10853-009-3613-6

MESOSTRUCTURED MATERIALS

SBA-15 modified with Al, Ti, or Zr as supports for highly active NiW catalysts for HDS

Lilia Y. Lizama · Tatiana E. Klimova

Received: 26 November 2008 / Accepted: 16 May 2009 / Published online: 2 June 2009

Abstract A series of SBA-15-type materials modified with Al, Ti, and Zr were prepared and used as supports for hydrodesulfurization (HDS) catalysts based on NiW. Prepared supports and catalysts were characterized by N_2 physisorption, small- and wide-angle XRD, UV–Vis DRS, FT-IR, IEP, TPR, TPD, HRTEM, and SEM–EDX. Sulfided catalysts were evaluated in HDS of dibenzothiophene (DBT). Catalytic activity tests show that the creation of defined anchoring points for the W species by modifying the surface of SBA-15 with Al, Ti, and Zr results in a considerable improvement in catalysts' performance compared to pure SBA-supported analog. The possible reasons for this behavior are discussed.

Introduction

The removal of sulfur from gasoline and diesel oil is strongly desirable in order to avoid the adverse environmental consequences of SO_x pollution and also to increase the durability of refinery equipment and minimize the sulfur poisoning of other catalytic systems that use noble metals [1–3]. This issue has driven most of the countries to create more stringent regulations for sulfur content since the last two decades. For this year, it has been proposed to switch from the currently accepted ultra low sulfur diesel (ULSD, $S < 50$ ppm) to sulfur-free diesel fuel (SFD, $S < 10$ ppm) [4].

L. Y. Lizama · T. E. Klimova (✉)
Facultad de Química, Universidad Nacional Autónoma de México, Cd. Universitaria, Coyoacán, 04510 México, DF, México
e-mail: klimova@servidor.unam.mx

Some of the emerging technologies and other key factors for the production of ultra-clean fuels are discussed in Refs. [1–5]. Among these novel approaches, it appears that the improvement of classical HDS-type processes will still be the most effective option for producing affordable fuels with sulfur levels of 10 ppm or slightly below [3, 5].

The development of new, improved HDS catalysts has been one of the focuses of academic and industrial research. As a result, a number of novel catalysts with improved activity and selectivity are already available in the market [1, 3]. However, in order to reach the ultra-low sulfur levels, the use of these new catalysts has to be combined with more severe operating conditions which result in higher capital investment due to both operational cost and loss in yield and product quality [2, 6]. Thus, the development of more active catalysts able to operate in a cost-effective manner is still a challenge for researchers.

In order to improve catalytic activity for deep HDS, design approaches have focused on the removal of sulfur from the most refractory molecules such as DBT and its alquilated derivatives; 4-methyldibenzothiophene (4-MDBT) and 4,6-dimethyldibenzothiophene (4,6-DMDBT) [7]. It is well known that NiW-based catalysts present some advantages in the conversion of hindered DBTs under severe conditions, due to their higher hydrogenation ability compared to NiMo or CoMo analogs [8, 9]. In addition to cost reasons, one of the drawbacks for using alumina-supported W-based catalysts in conventional HDS processes is the fact that their oxide precursors are more difficult to convert to the corresponding active sulfide species than the Mo-based analogs [8–11]. This behavior is a consequence of two main factors; the intrinsically strong W–O bonds in tungsten oxides, which are difficult to break and form the corresponding sulfides at temperatures below 400 °C [12] and the relatively strong interaction of the

tungsten oxides with the alumina support via W–O–Al bonds, which makes these species even harder to fully sulfide [13].

Targeting the second issue, a number of different supports (i.e., TiO_2 [14], HMS [15], carbon [9], etc.) have been proposed as promising alternatives to the strongly interacting alumina for NiW catalysts. In a recent work [16], we tested SBA-15 as carrier for NiW catalysts, resulting in the formation of WO_x species susceptible to be reduced at lower temperatures than the ones present on their alumina-supported analogs, which caused an increased activity in HDS of 4,6-DMDBT. It is worth mentioning that these good results were obtained with purely siliceous SBA-15, even though it is well-known that the low density of OH groups on silica surface leads to weak interactions among silica and Mo (or W) species, thus, inhomogeneity of the sulfide species normally prevails [17].

In order to improve the interaction of purely siliceous mesoporous materials with NiMo oxide and sulfide species, we started testing Al-modified MCM-41 [18] materials as supports for HDS catalysts, showing catalytic activity comparable to conventional catalysts. However, the poor stability of MCM-type materials represents a serious limitation to its practical use. In the seek for more stable materials and better textural properties, we tested Al-SBA-16 [19] and Ti-SBA-16 [20] as supports for NiMo catalysts, showing promising results in HDS of hindered DBTs. Further increase in HDS activity was observed when SBA-16 was replaced by SBA-15, support with hexagonal arrangement of cylindrical mesopores of larger size than in SBA-16. Thus, Al-SBA-15 [21], Ti-SBA-15 [22], and Zr-SBA-15 [23] supports have shown to enhance catalytic activity of NiMo-based catalysts by increasing the dispersion of the oxide species, which leads to dispersed and homogenous active sulfide phases. Similar results for NiMo- and CoMo-based catalysts can be found in Refs. [24–26].

In the seek to improve the catalyst performance by having a better control on the dispersion of the active NiW phase, the present work is aimed at the synthesis of homogeneous oxide and sulfide species by means of the incorporation of anchoring sites (Al, Ti, or Zr) on the SBA-15 support surface together with the use of Keggin-type $H_3PW_{12}O_{40}$, an aggregate with well-defined size and shape, as precursor.

Experimental

Synthesis of supports and catalysts

The pure siliceous hexagonal *p6mm* SBA-15 was prepared according to literature [27, 28] using the triblock copolymer Pluronic P123 ($M_{av} = 5800$, $EO_{20}PO_{70}EO_{20}$, Aldrich) as the structure-directing agent and tetraethyl orthosilicate (TEOS, Aldrich, 99.999%) as the silica source. Pluronic P123 (4 g) was dissolved in water (30 g) and 2 M HCl (120 g) solution at 35 °C. Then TEOS (8.5 g) was added into the solution. The mixture was stirred at 35 °C for 20 h and then aged at 80 °C for 48 h without stirring. The solid product was recovered by filtration, washed with deionized water and air-dried at room temperature. Calcination was carried out at 550 °C for 6 h. Modified SBA-15 supports, hereinafter referred to as M-SBA where M = Al, Ti or Zr, were prepared by chemical grafting using anhydrous ethanol (EtOH, Aldrich, 99.999%) as solvent in all cases and aluminum(III) chloride ($AlCl_3$, Aldrich 99.999%), titanium(IV) isopropoxide (Ti(i-PrO)$_4$, Aldrich, 97%), and zirconium(IV) propoxide, (Zr(*n*-PrO)$_4$, Fluka, 70 wt% solution in 1-propanol) as M sources. The typical synthetic procedure was as follows: 1 g of SBA-15 was slurried in 200 mL of anhydrous ethanol containing an excess of the corresponding M-precursor for 8 h at room temperature. The resulting filtered materials were rinsed with anhydrous ethanol, dried at room temperature and calcined at 550 °C for 5 h. Catalysts were prepared by W incorporation to M-SBA supports as well as to a reference pure SBA carrier by incipient wetness impregnation of methanol solutions of Keggin-type heteropolyacid, $H_3PW_{12}O_{40} \cdot xH_2O$ (HPA, Sigma-Aldrich). The promoter was incorporated in a second step by impregnation of methanol solution of nickel nitrate, $Ni(NO_3)_2 \cdot 6H_2O$ (Baker). After each impregnation, the samples were calcined for 2 h at 350 °C. The samples were designated as W/(M-)SBA for unpromoted catalysts and NiW/(M-)SBA for promoted catalysts. The nominal composition of the catalysts was 9.5 wt% of W and 2.4 wt% of Ni. A reference catalyst, NiW/Al_2O_3, was prepared from the HPA precursor ($H_3PW_{12}O_{40} \cdot xH_2O$, Sigma-Aldrich) supported on a conventional carrier (γ-alumina from pseudo-boehmite Catapal B calcined at 700 °C for 4 h). The impregnation and calcination procedures, as well as the catalyst's loading were the same as the ones described for the (M)-SBA-supported catalysts.

Characterization

The supports and catalysts were characterized by N_2 physisorption, small- and wide-angle X-ray diffraction (XRD), isoelectric point (IEP), UV–vis diffuse reflectance spectroscopy (DRS), FT-IR, temperature-programmed reduction (TPR), NH_3 temperature-programmed desorption (TPD), HRTEM, and chemical analysis (SEM–EDX). N_2 adsorption/desorption isotherms were measured with a Micromeritics ASAP 2000 automatic analyzer at liquid N_2 temperature. Prior to the experiments, the samples were degassed ($P < 10^{-1}$ Pa) at 270 °C for 6 h. Specific surface areas (S_{BET}) were calculated by the BET method and the

pore volume (V_p) was determined by nitrogen adsorption at a relative pressure of 0.98. The mesopore diameter (D_p) corresponds to the maximum of the pore size distributions obtained from the adsorption isotherms by the BJH method. The micropore area (S_μ) was estimated using the correlation of *t*-Harkins & Jura (*t*-plot method). XRD patterns were recorded in the $3^\circ \leq 2\theta \leq 90^\circ$ range in a Siemens D5000 diffractometer, using CuKα radiation ($\lambda = 1.5406$ Å) and a goniometer speed of 1° (2θ) min^{-1}. Small-angle XRD ($2\theta = 0.5$–10°) was performed on the Bruker D8 Advance diffractometer using small divergence and scattering slits of 0.05°. The a_0 unit-cell parameter was estimated from the position of the (1 0 0) diffraction line $\left(a_0 = d_{100} \times 2/\sqrt{3}\right)$. Pore wall thickness, δ, was assessed as in [29] by subtracting D_p from the a_0 unit-cell parameter which corresponds to the distance between centers of adjacent mesopores. The measurements of zeta potential of SBA-15-type supports were carried out at different pH values in a Zeta-Meter 3.0+ instrument. Isoelectric point (IEP) was determined as the pH value at which zeta potential of the particles equaled 0. UV–Vis electronic spectra of the samples were recorded in the wavelength range 200–800 nm using a Varian Cary 100 spectrophotometer equipped with a diffuse reflectance attachment. Polytetrafluoroethylene was used as reference. IR spectra of the supports and catalysts were recorded after transfer in air, in an absorbance mode with a Perkin-Elmer FTIR 1605 Fourier transform spectrometer. NH_3 TPD and TPR experiments were carried out in a Micromeritics AutoChem II 2920 automatic analyzer equipped with a TC detector. Before ammonia adsorption, the samples were pretreated in situ at 500 °C for 30 min in a helium flow in order to remove water and other contaminants. The samples were then cooled to 120 °C and contacted with a He/NH_3 mixture (90/10 v/v) at a flow rate of 20 mL/min for 30 min. The desorption step was performed in a He stream (50 mL/min) with a heating rate of 10 °C/min. After reaching 500 °C, the sample was kept at this temperature until the trace reached the base line. In the TPR experiments, the samples were pretreated in situ at 350 °C for 2 h under air flow and cooled in an Ar stream. The reduction step was performed under a stream of Ar/H_2 mixture (90/10 mol/mol and 50 mL/min), with a heating rate of 10 °C/min, up to 1000 °C. High-resolution transmission electron microscopy (HRTEM) studies were performed using a JEOL 2010 microscope (resolving power 1.9 Å). The solids were ultrasonically dispersed in heptane and the suspension was collected on carbon-coated grids. Layer stacking distributions and slab length of WS_2 crystallites in each sample were established from the measurement of at least 300 crystallites detected on several HRTEM pictures taken from different regions of each sample. Chemical composition of the supports was determined by SEM–EDX using JEOL 5900 LV microscope with OXFORD ISIS equipment.

Catalytic activity tests

Prior to the catalytic activity tests, the catalysts were sulfided ex situ in a tubular reactor at 400 °C for 4 h in a stream of 15 vol% of H_2S in H_2 under atmospheric pressure. The catalytic activity tests were performed in a batch reactor (Parr) at 300 °C and 7.3 MPa total pressure for 8 h. The reactor was filled in an inert atmosphere with 40 mL of a solution of DBT in hexadecane (with a sulfur content of 1300 ppm) and 0.15 g of sulfided catalysts. The course of the reaction was followed by taking aliquots each hour and analyzing them in an HP-6890 chromatograph equipped with a FID detector and a non-polar methyl siloxane capillary column HP-1 (50 m × 0.32 mm i.d. and 0.52 μm film thickness). To corroborate liquid product identification, the product mixture was analyzed in a Hewlett Packard GC-MS equipment. The identified reaction products were 1,2,3,4-tetrahydrodibenzothiophene (THDBT), 1,1′-cyclohexylbenzene (CHB), 1,1′-bicyclohexyl (BCH), and 1,1′-biphenyl (BP). The quantitative analysis of the reactant and products was performed using corresponding calibration curves and hexadecane as an internal standard in all cases.

Results and discussion

Characterization of supports

The chemical compositions of the synthesized supports are given in Table 1. As the incorporation of the heteroatoms by the grafting procedure is expected to happen by their retention on the surface only via M–O–Si linkages, it can be said that the saturation of the surface of the SBA-15 was reached at 10 wt% of Al_2O_3, 16 wt% of TiO_2, and 22 wt% of ZrO_2 which are close to the results found elsewhere [30, 31]. In the three cases, the resulting values of monolayer capacity of SBA-15 were close to 2 M atoms/nm^2, which is below the well-known silanol surface density of SBA-15 ($\sim$3.7 OH/nm^2) [32]. This can be explained by the existence of some silanol groups which did not react with the different precursors at room temperature, as it has previously been observed for different silica-based materials [33].

The values of isoelectric point (IEP) determined for Ti- and Zr-modified supports are shown in Table 1. The value of IEP for siliceous SBA-15 parent support suffers a basic shift from 2.1 to 3.1 after titania incorporation, which is an intermediate value between those of the two pure oxides, as

Table 1 Composition, textural characteristics, and isoelectric point of supports

Sample	SiO_2[a] (wt%)	M_xO_y[a] (wt%)	Atoms of M per nm^2	S_{BET}[b] (m^2/g)	NS_{BET}[c]	S_μ[d] (m^2/g)	V_p[e] (cm^3/g)	D_p[f] (Å)	δ[g] (Å)	IEP[h] (pH)
SBA	100	–	–	832	1	141	1.11	86	20	2.1
Al-SBA	90	10	2.0	592	0.79	86	0.84	80	26	n.d.
Ti-SBA	84	16	2.1	560	0.80	77	0.79	75	31	3.1
Zr-SBA	78	22	1.9	585	0.90	97	0.77	75	31	3.7

[a] Determined by SEM-EDX

[b] Specific surface area

[c] Normalized surface area calculated as $NS_{BET} = S_{BET,\ M\text{-}SBA}/S_{BET,\ SBA}(1 - y)$ where y is the weight fraction of M_xO_y in the support

[d] Micropore area

[e] Total pore volume

[f] Pore diameter determined from the adsorption branch of the N_2 physisorption isotherm

[g] Pore wall thickness calculated as $\delta = a_0 - D_p$

[h] Isoelectric point

titania's IEP is equal to 5.4. A similar effect is observed for Zr-modified support, where the IEP is 3.7, which is relatively close to the value of 4.3, characteristic of pure ZrO_2.

The nitrogen adsorption–desorption isotherms for the supports are shown in Fig. 1. All isotherms correspond to type IV and exhibit an H1 hysteresis loop characteristic of SBA-15 mesoporous material. The sharpness of the adsorption branches is indicative of a narrow mesopore size distribution in all cases.

The textural characterization results (Table 1) show that the incorporation of Al, Ti, and Zr to the SBA-15 matrix produces a decrease in specific surface area (S_{BET}), micropore area (S_μ), and pore volume (V_p). This result is mainly caused by the increase in the materials' density due to the incorporation of the M oxides, but a slight pore blockage cannot be ruled out as inferred from the values of normalized surface area (NS_{BET}), especially for Al-SBA and Ti-SBA supports. The decrease in pore diameter (D_p) from 86 Å for pure SBA to 75–80 Å for modified supports, together with the increase in the pore wall thickness (d) indicate that the metal oxide species are located inside the pores.

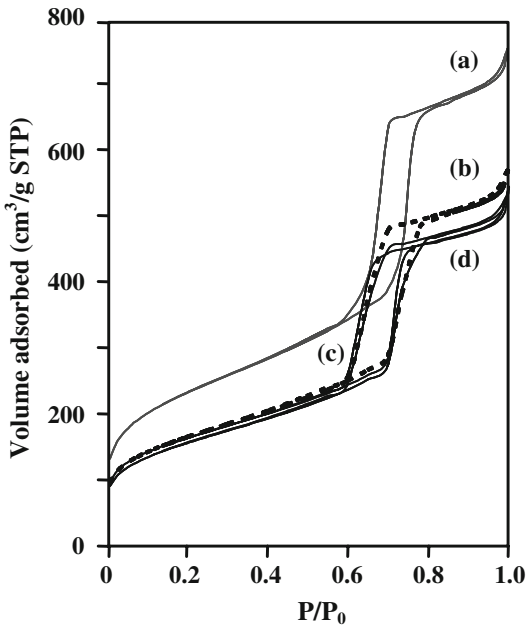

Fig. 1 Nitrogen adsorption–desorption isotherms of SBA (*a*), Al-SBA (*b*), Ti-SBA (*c*), and Zr-SBA (*d*)

The small-angle XRD patterns of the supports are shown in Fig. 2. All samples exhibit three clearly defined peaks characteristic of hexagonally ordered *p6mm* structure; a strong (1 0 0) reflection at 0.96° (2θ) and two small shoulders between 1.5° and 2° (2θ) which yield an a_0 value of 106 Å. Even though the position of the reflections did not change, the intensity of the signals suffers a minor decrease especially in the case of the Zr-SBA support, showing that the hexagonal array of pores was preserved but there might be a slight loss in the long-range periodicity of the supports when increasing the metal oxide content. Wide-angle XRD of the supports (not shown) demonstrated that deposited metal oxide species are well-dispersed in all samples, as no crystalline phases were detected.

The IR spectra of the supports are shown in Fig. 3. The four spectra show similar overall characteristics, resulting from a typical siliceous material. The main vibration band at ca. 1080 cm^{-1}, as well as the small shoulder at ca. 1220 cm^{-1} can be assigned to Si–O–Si asymmetric stretching modes. A shift of the main band to lower wavenumbers (ca. 1072 cm^{-1}) is observed for the modified supports, which can be considered as an indication of the incorporation of the cations into the framework of the siliceous mesoporous material [31, 34]. A weak band can be observed at 800 cm^{-1} due to Si–O–Si symmetric stretching modes and a strong band appears at 458 cm^{-1}, due to rocking Si–O–Si. The band at ca. 960 cm^{-1} has

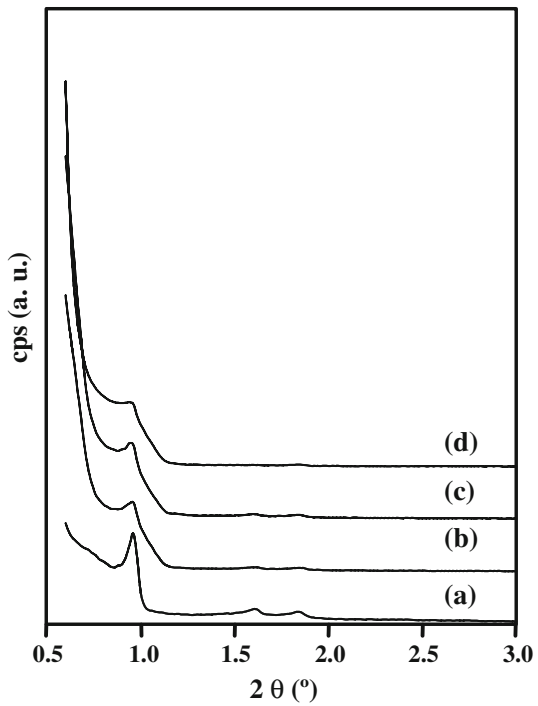

Fig. 2 Small-angle XRD patterns of SBA (*a*), Al-SBA (*b*), Ti-SBA (*c*), and Zr-SBA (*d*)

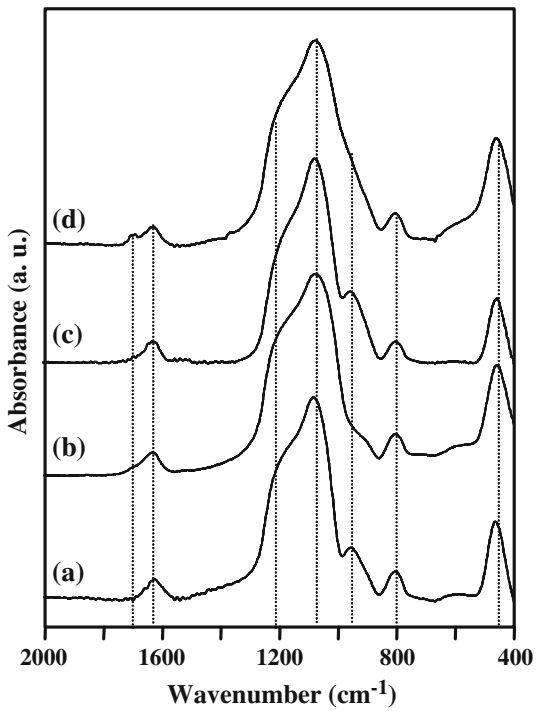

Fig. 3 IR spectra of SBA (*a*), Al-SBA (*b*), Ti-SBA (*c*), and Zr-SBA (*d*)

been assigned to the Si–O stretching vibrations of Si–O–R groups, where R = H in the case of pure siliceous materials [34] but it is also observed when R = Ti, Zr, Ce among others [31, 34–37]. As a result of the post-synthetic incorporation of Al, Ti, and Zr species, which proceeds via a condensation process of the corresponding M alkoxides with Si–OH terminal groups, the band at 960 cm^{-1} suffers some changes in intensity and position depending on the nature of the grafted metal. In the case of Al-modified support, this signal shows a decrease in intensity, which is in agreement with previously published results [31, 38, 39]. The Ti-SBA spectrum exhibits a more intense band at 960 cm^{-1} compared to the one of the SBA-15 sample, which has been widely taken as a proof of Ti incorporation to the silica matrix as the band assigned to Si–O–Ti bond vibrations appears at that same position [35, 40–43]. In the spectrum of Zr-SBA, the main line (1072 cm^{-1}) of the stretching vibrations of Si–O–Si suffers a broadening due to the superimposition with Si–O–Zr bonds, which produces a signal at ca. 984 cm^{-1} [44–47]. The new broad absorption around 600 cm^{-1} can be assigned to Zr–O bending [47].

UV–vis diffuse reflectance spectra of the different supports are presented in Fig. 4. Pure SBA and Al-SBA supports do not show any absorption bands as they are transparent in this region of the UV–vis spectrum, but useful information can be obtained for Ti- and Zr-modified SBA samples by this technique. Since both Ti^{4+} and Zr^{4+} have a d^0 electronic configuration, only one absorption is observed due to ligand-to-metal charge transfer (LMCT) $O^{2-} \rightarrow M^{4+}$ [48, 49]. According to the literature, bulk anatase TiO_2 exhibits a broad absorption with maximum at

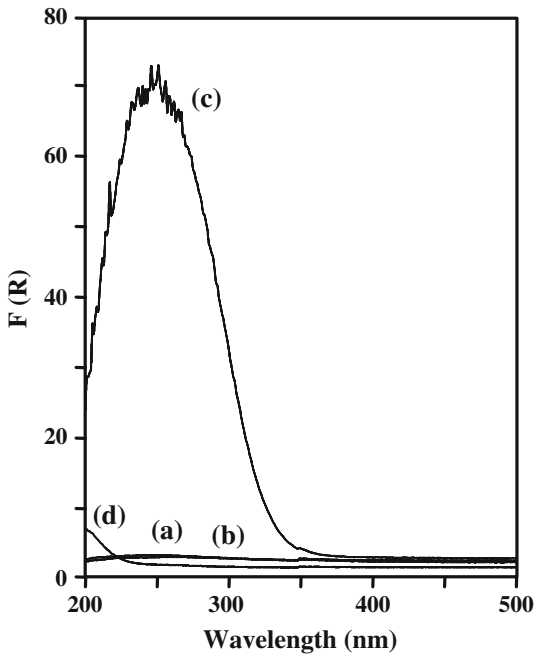

Fig. 4 UV–vis diffuse reflectance spectra of SBA (*a*), Al-SBA (*b*), Ti-SBA (*c*), and Zr-SBA (*d*)

330 nm and band gap of ca. 3.3 eV, while the transition around 220–230 nm with absorption edge of ~4.7 eV is assigned to Ti in isolated tetrahedral sites [43, 48–51]. The spectrum of Ti-SBA (Fig. 4c) support shows a broad absorption over the 220–340 nm range with maximum at 250 nm, characteristic of Ti-modified SBA-15 within similar TiO_2 loadings [23, 50, 52]. It is well known that the UV absorption edge or optical band-gap, E_g, is a strong function of the TiO_2 particle size with diameters less than 4 nm [49]. The E_g value obtained for Ti-SBA sample was 3.9 eV, presenting a blue shift from the value of pure bulk anatase, which, corroborated with XRD results, allows us to confirm a good dispersion of the Ti species in the SBA-15 matrix, where both isolated Ti species with tetrahedral coordination but also partially polymerized Ti entities with octahedral coordination (small Ti–O–Ti clusters) coexist.

The UV–vis diffuse reflectance spectrum of Zr-SBA shows the characteristic absorption with maximum at about 200 nm, attributable to MLCT involving pure Zr(IV) with tetrahedral configuration, while no absorption can be observed in the 240–310 nm range, totally ruling out the presence of other ZrO_2 high-temperature polymorphs [23, 49, 53, 54]. The absorption edge for this sample, 5.5 eV, was larger than the E_g reported for pure tetragonal zirconia (5.2 eV), suggesting that the ZrO_2 species are present as small particles on the surface of the SBA-15.

Characterization of catalysts

The nitrogen adsorption–desorption isotherms for NiW catalysts are shown in Fig. 5. All isotherms preserve the characteristic shape of SBA-15 mesoporous material, even after the incorporation of all the metal oxide phases. The textural characterization results (Table 2) show that the addition of W and Ni oxides produces a decrease in specific surface area (S_{BET}), micropore area (S_μ), and pore volume (V_p) which, once again, is mostly caused by the increase in the materials' density but also by pore blockage in a minor quantity. The decrease in pore diameter (D_p) is also indicative of the presence of the incorporated oxides inside the pores.

Powder X-ray diffractograms for NiW catalysts are shown in Fig. 6. The broad and only signal present in all samples is caused by the amorphous silica walls of the SBA-15 material. These results confirm the absence of any crystalline phase, indicating a good dispersion of all metal oxides incorporated to the SBA-15 parent support.

Reduction profiles of NiW catalysts and pure $H_3PW_{12}O_{40}$ are presented in Fig. 7 and the H_2 consumption recorded for each sample is shown in Table 3. Additionally, reduction profiles of NiW reference samples supported on the pure oxides (i.e., Al_2O_3, TiO_2, and ZrO_2) are shown in Fig. 8. Exact assignment of these TPR signals is

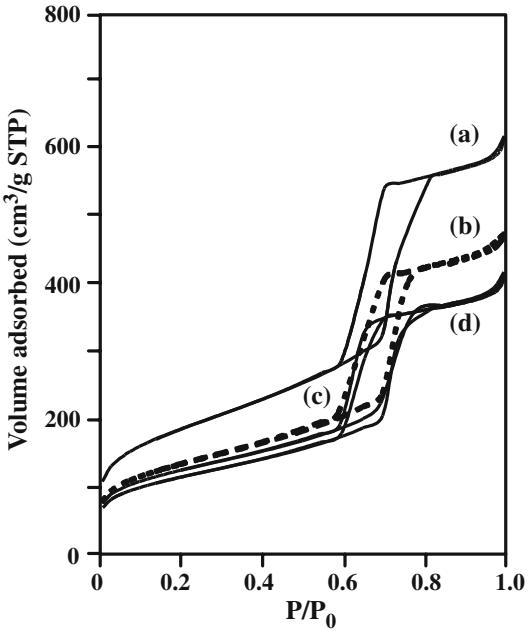

Fig. 5 Nitrogen adsorption–desorption isotherms of NiW catalysts supported on SBA (*a*), Al-SBA (*b*), Ti-SBA (*c*), and Zr-SBA (*d*)

Table 2 Textural characteristics of catalysts

Sample	S_{BET}[a] (m^2/g)	NS_{BET}[b]	S_μ[c] (m^2/g)	V_p[d] (cm^3/g)	D_p[e] (Å)
W/SBA	720	0.99	104	0.97	75
NiW/SBA	663	0.94	108	0.92	73
W/Al-SBA	511	0.99	72	0.76	78
NiW/Al-SBA	487	0.95	72	0.70	75
W/Ti-SBA	433	0.88	74	0.62	75
NiW/Ti-SBA	409	0.86	69	0.61	75
W/Zr-SBA	456	0.89	94	0.60	75
NiW/Zr-SBA	444	0.90	82	0.60	75

[a] Specific surface area

[b] Normalized surface area calculated as $NS_{BET} = S_{BET,\,(Ni)W/(M\text{-})SBA}/S_{BET,\,(M\text{-})SBA}(1-y)$ where y is the weight fraction of Ni and/or W oxides incorporated to each support

[c] Micropore area

[d] Total pore volume

[e] Pore diameter determined from the adsorption branch of the N_2 physisorption isotherm

complicated because of the complex character of the reduction process of W^{6+} oxide species, which proceeds through different intermediate oxidation states, depending on the reduction conditions, support, etc. [55, 56].

According to the literature, the reduction for bulk-like tungsten oxide species proceeds through three main steps: from WO_3 to $WO_{3-x,(0<x<1)}$ around 540 °C, where WO_{3-x} could correspond to a variety of suboxides ($W_{20}O_{58}$, $W_{18}O_{49}$, $W_{24}O_{68}$…[57]), from $WO_{3-x,(0<x<1)}$ to WO_2 at

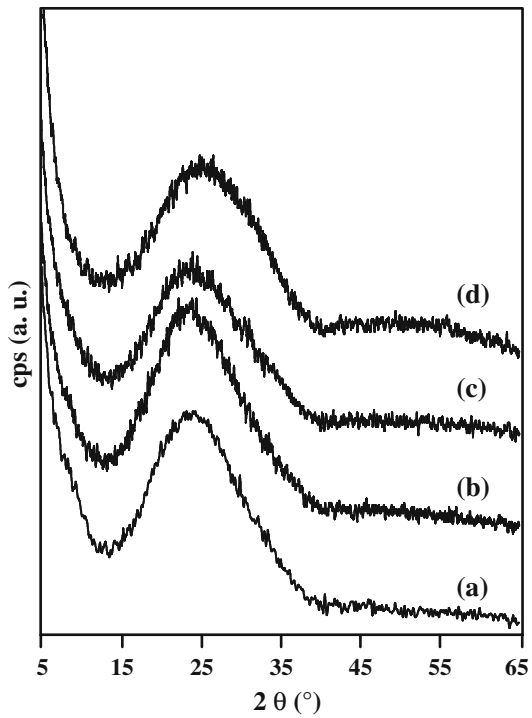

Fig. 6 XRD patterns of NiW catalysts supported on SBA (*a*), Al-SBA (*b*), Ti-SBA (*c*), and Zr-SBA (*d*)

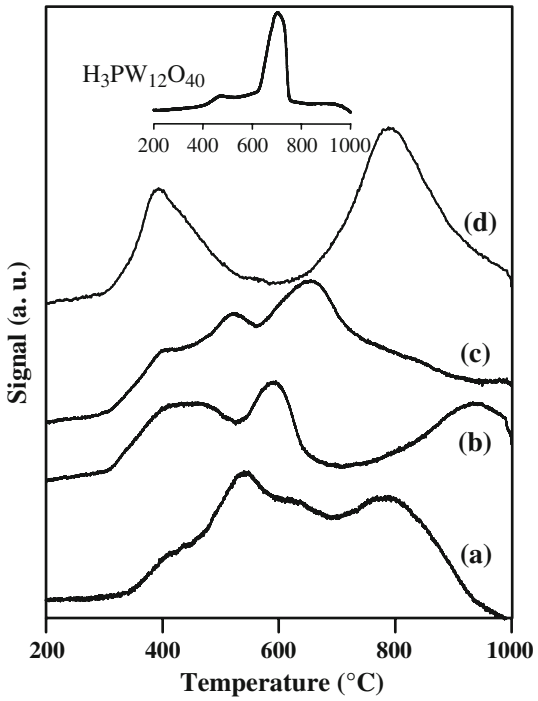

Fig. 7 TPR profiles of NiW catalysts supported on SBA (*a*), Al-SBA (*b*), Ti-SBA (*c*), and Zr-SBA (*d*)

temperatures around 750 °C and WO_2 to W^0 at temperatures higher than 900 °C [58, 59]. For the case of WO_3 species dispersed on a support, it has been found that octahedrally coordinated WO_x species are reduced at temperatures varying from 300 to 600 °C [55], while tetrahedrally coordinated isolated or dimeric WO_x species with strong interaction with supports like Al_2O_3 are more difficult to reduce, requiring temperatures around 900–1000 °C [55–57, 59].

For the parent $H_3PW_{12}O_{40}$ acid, two main peaks are observed. The first one at ca. 477 °C can be attributed to the loss of framework oxygen by the Keggin unit prior to its decomposition [60, 61]. The hydrogen uptake above 600 °C indicates the reduction of WO_3-like species, product of the decomposition of the parent HPA. For NiW catalysts, it can be clearly noticed that the number and ease of reduction of the deposited Ni and W oxides strongly depend on the nature of the support. However, all catalysts feature a low-temperature H_2 uptake with different intensities but with the same maximum at ~400 °C, which can be attributed to the presence of nickelpolytungtate-like phases [8]. The most heterogeneous distribution of species is found on pure SBA-supported catalyst, in which W oxide species with different degrees of agglomeration give place to an undefined reduction profile. For the NiW/Al-SBA catalyst, the H_2 consumption in the 450–600 °C region can be attributed to disperse polytungstate species with different degrees of reducibility [8, 10]. The high temperature signal above 850 °C reflects the presence of some W-containing species hard to reduce due to the interaction with the Al-modified support via Al–O–W linkages, as observed for alumina-supported NiW catalysts [61]. In the case of Ti-SBA-supported catalyst, the peaks located at ~530 °C and 660 °C can also be attributed to the presence of octahedrally coordinated polytungstate species. A homogenous distribution of NiW oxide species can be inferred for the Zr-SBA-supported catalyst by the defined reduction profile in which two defined peaks appear. The peak at ca. 400 °C shows that, compared to the other catalysts, NiW/Zr-SBA sample has a larger proportion of homogenously dispersed polytungstate and/or nickel-polytungstate species susceptible of reducing at lower temperatures. The second peak at ~790 °C could correspond to the further reduction of species formed in the first step.

Ammonia TPD characterization results are shown in Table 3. NiW/SBA catalyst has the lowest density of surface acid sites among all samples. NiW/Ti-SBA shows the lowest acidity of the M-SBA-supported catalysts, presenting mostly weak and medium acid sites. NiW/Al- and Zr-SBA samples present the highest acidity and a similar behavior in the number and strength of acid sites. However, the difference in the nature of acid sites (i.e., Brönsted or Lewis) can be expected for these two supports. Based on the results of our previous work [21], we expect NiW/Al-SBA to present a mixture of Brönsted and Lewis acid

Table 3 Quantitative analysis of TPR and ammonia TPD results obtained for NiW catalysts

Catalyst	TPR		NH_3 TPD				
	Peak max. (°C)	H_2 consumption (mL/g STP)	Acid sites density (μmol NH_3/m^2)	Amount of acid sites (μmol NH_3/g)			
				Total	Weak (120–200 °C)	Medium (200–400 °C)	Strong (400–500 °C)
NiW/SBA	410	4	1.1	733	147	312	274
	546	16					
	793	13					
NiW/Al-SBA	443	17	2.3	1,131	278	562	291
	594	10					
	934	16					
NiW/Ti-SBA	404	7	1.7	700	264	285	151
	531	10					
	651	15					
	898	6					
NiW/Zr-SBA	379	14	2.8	1,144	333	561	250
	792	28					

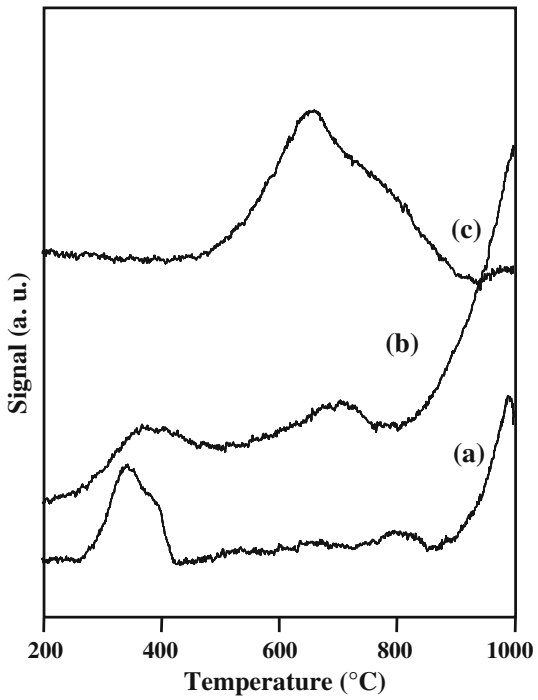

Fig. 8 TPR profiles of reference NiW catalysts supported on Al_2O_3 (*a*), TiO_2 (*b*), and ZrO_2 (*c*)

sites, where the first ones are well known to participate in isomerization and cracking reactions in HDS tests as it was shown for NiMo catalysts supported on Al-modified mesoporous silicas [18, 19, 21]. Acid sites on the NiW/Zr-SBA sample are expected to be only of Lewis type as reported by Tuel [62], who characterized Zr-HMS materials with a similar composition as ours by IR spectroscopy of adsorbed pyridine and observed only Lewis and no Brönsted acid sites.

In order to get information about the dispersion of the activated catalysts, HRTEM studies were performed. The typical fringes due to WS_2 crystallites with 6.2 Å interplanar distances were observed on micrographs of all sulfided catalysts (Fig. 9), showing that the oxide precursors were transformed during the sulfidation stage to the sulfided W phase with regular structure. This transformation can be corroborated by comparing the micrographs of the sulfided catalysts with the corresponding ones of the oxided catalysts (not shown). The distributions in stacking degree and slab length for the different catalysts are presented in Fig. 10. All sulfided catalysts supported on M-modified SBA show a better dispersion (smaller average stacking degree and slab length) than the NiW/SBA sample, which shows a heterogeneous distribution of sulfide crystallites ranging from 20 to more than 60 Å in length and an average stacking of 4 layers. Even though the average stacking degree (~2.5 layers) and average slab length (~30 Å) are very similar among the NiW/M-SBA series, it can be noticed (Fig. 10) that the narrowest distribution of species is found in NiW/Zr-SBA catalyst, which is in close agreement with the TPR characterization of the catalyst prior to its activation. The reference catalyst, NiW/Al_2O_3 showed a low degree of stacking, mostly consisting of crystals with one or two slabs, but the average slab length was considerably higher (~55 Å) than in any other sample in this series, which is a consequence of the strong interaction of the alumina support with the W species in the oxide and sulfide forms [8–11, 13].

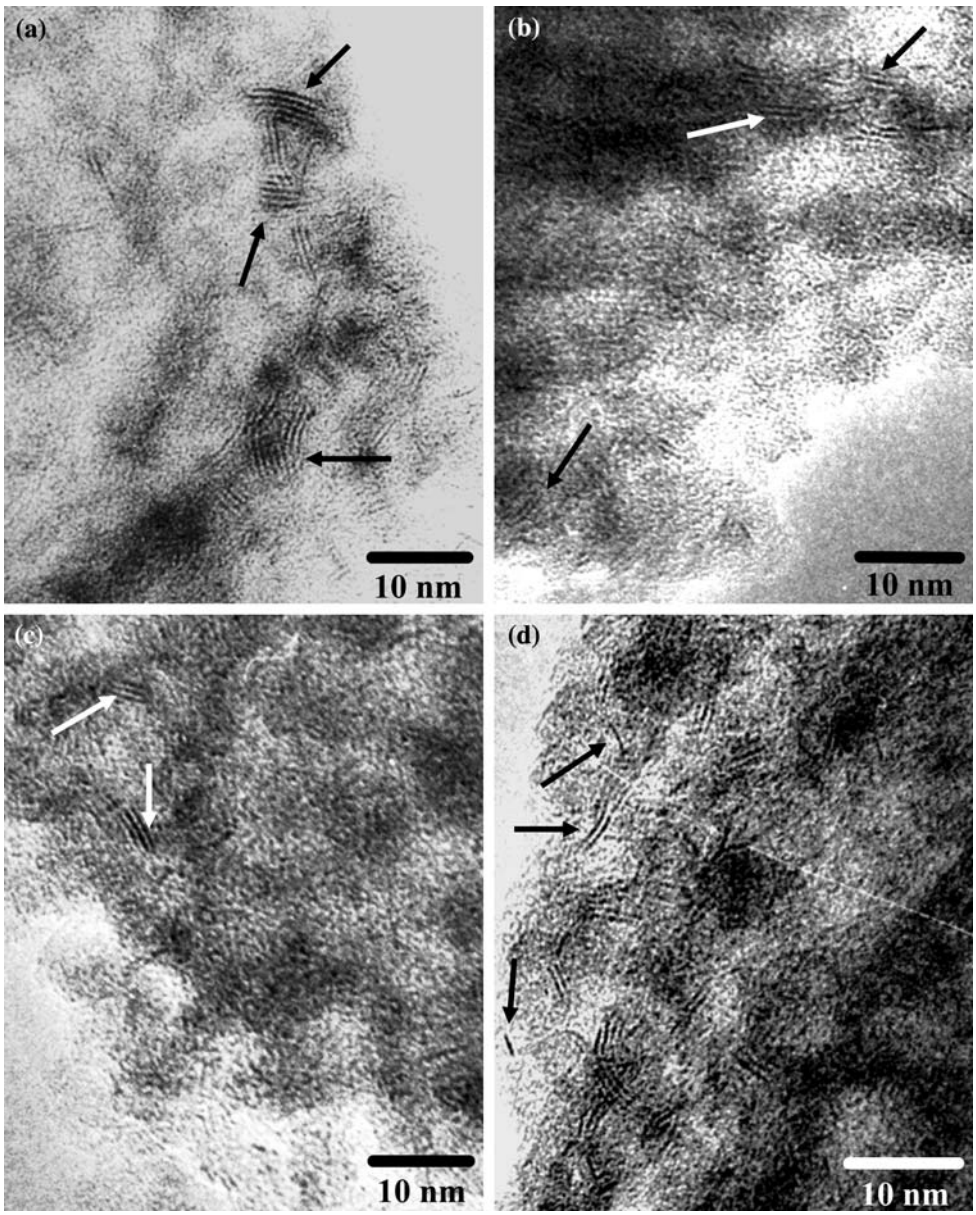

Fig. 9 HRTEM micrographs of sulfided NiW catalysts supported on SBA (**a**), Al-SBA (**b**), Ti-SBA (**c**), and Zr-SBA (**d**)

Catalytic activity

The conversions of DBT obtained over sulfided NiW/(M-)SBA catalysts, as well as over reference NiW/Al_2O_3 catalyst are shown in Fig. 11. Pseudo-first-order rate constants (k_1 expressed in L/(s × $g_{catalyst}$)) were calculated as described in [63, 64] and are shown in Table 4, together with the initial reaction rates (r_0 in [mol/(L × h × $g_{catalyst}$)]). Catalytic activities of all SBA-supported catalysts resulted to be substantially higher than that of the reference alumina-supported catalyst, which showed a conversion of 70% at 8 h. The three NiW/M-SBA catalysts reached almost 100% of DBT conversion within 8 h, which was about 10 % higher than the pure SBA-supported catalyst. Pseudo-first-order rate constants determined for the different catalysts vary between 6.9 × 10^{-6} and 2.2 × 10^{-5} L/(s × $g_{catalyst}$) and also confirm the following order of activity; NiW/Al_2O_3 < NiW/SBA < NiW/Al-SBA < NiW/Ti-SBA = NiW/Zr-SBA.

Generally, there are two reaction pathways for the HDS of DBT. The first one is the direct elimination of the sulfur atom from the molecule (DDS route) yielding the corresponding biphenyl product and the second one is the prehydrogenation of one of the aromatic rings followed by the elimination of the sulfur atom (HYD route), yielding first tetrahydrodibenzothiophene and then the corresponding cyclohexylbenzene-type compounds [7]. As usually reported ([18] and references therein) it is considered that

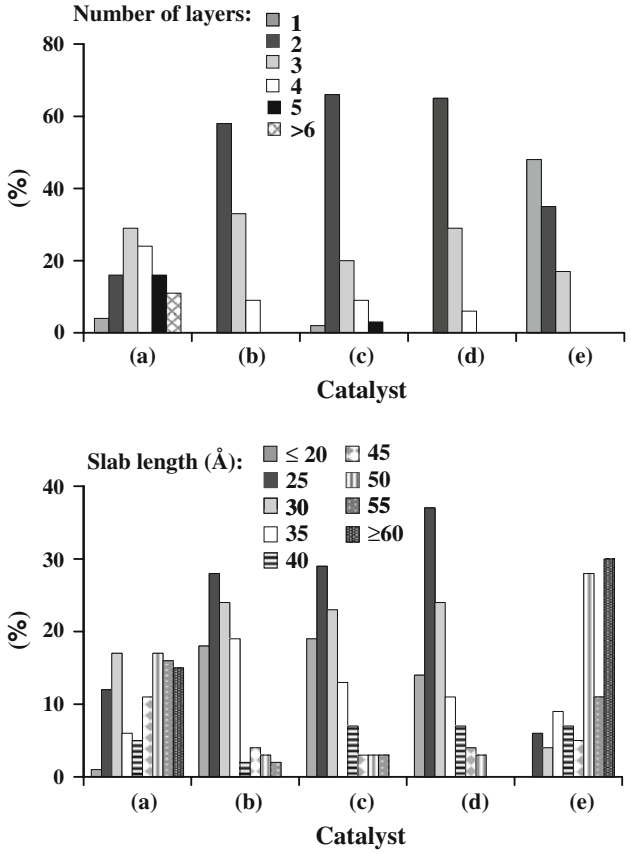

Fig. 10 Layer stacking and length distribution of WS_2 crystallites in sulfided NiW catalysts supported on SBA (*a*), Al-SBA (*b*), Ti-SBA (*c*), Zr-SBA (*d*), and reference catalyst NiW/Al_2O_3 (*e*)

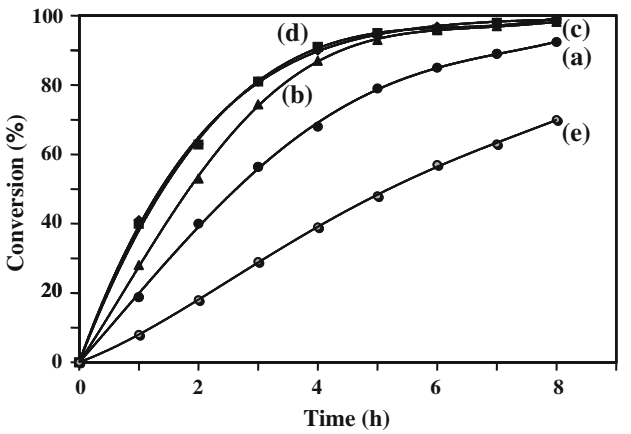

Fig. 11 DBT conversions obtained over NiW catalysts supported on SBA (*a*), Al-SBA (*b*), Ti-SBA (*c*), Zr-SBA (*d*), and reference catalyst NiW/Al_2O_3 (*e*)

biphenyl practically does not transform into cyclohexylbenzene; therefore, it is assumed that cyclohexylbenzene is mostly produced from tetrahydrodibenzothiophene.

In order to elucidate the effect of the support on the reaction pathways of HDS of DBT, the reaction product distributions at the same total conversion (40%) were compared for the different catalysts (Table 4). The HYD/DDS ratios determined as the ratios of the main desulfurized products obtained in each route (cyclohexylbenzene/biphenyl, respectively) show that for all catalysts studied the preferential route is DDS. However, it can be noticed that the proportion of products obtained from each route varies depending on the support used, giving the following order of hydrogenation ability; $NiW/Al_2O_3 < NiW/SBA \approx NiW/Al\text{-}SBA < NiW/Ti\text{-}SBA \approx NiW/Zr\text{-}SBA$, which is very similar to the one observed for catalytic activity. These results suggest that the use of M-modified SBA materials as supports for HDS catalysts leads to an improvement in the hydrogenation ability of the catalyst, enhancing HYD route which results in an overall increase in the rate of DBT HDS. However, in the case of Al-SBA-supported catalyst, new products are formed in the reaction as a result of further transformations of biphenyl, cyclohexylbenzene and bicyclohexyl on the well known acid sites of the Al-modified mesoporous silicas as reported in previous works [18, 19, 21]. Even if a good overall activity was achieved on NiW/Al-SBA catalyst, the formation of these cracking products, i.e., benzene, cyclohexane, and lighter molecules (C_3–C_6) represents a decrease in liquid yield of the reaction and a loss of product quality.

Clearly, the outstanding performance of the sulfided NiW/Ti-SBA and NiW/Zr-SBA catalysts on the HDS reaction of DBT must be related to the characteristics of the support and the oxidic precursor phases outlined above. According to the results of characterization of the sulfided catalysts by HRTEM, a good dispersion of metal species in the oxide state of the catalyst leads to better dispersed active phases, which is a necessary condition for the creation of a larger amount of accessible active sites, improving catalytic activity. For NiW/Ti-SBA and NiW/Zr-SBA catalysts, the most homogenous distribution of WS_2 crystals was obtained (Figs. 9 and 10). These sulfides consist mostly of short slabs (25–30 Å) of 2 or 3 layers, which have been observed to feature a more favorable length/layer stacking ratio for HDS than the one found for the regular NiW/Al_2O_3 catalyst, in which the smaller proportion of oxide species susceptible to be activated at the sulfidation temperature used (400 °C), yield long (~50 Å) one or two layered slabs.

It has been observed [17] that for large molecules like dibenzothiophene, a very low degree of stacking, as in the case of alumina-supported catalysts, hampers the planar adsorption of the molecule through the aromatic rings decreasing the intrinsic HYD rate constant, which is also in agreement with our own observations from previous works [16, 18–23]. On the other hand, a very high degree of stacking, observed with weakly interacting supports (c.a. pure SBA), reduces the number of corner sites which are

Table 4 Initial reaction rates (r_0), pseudo-first order rate constants (k_1), and HYD/DDS pathway ratios obtained for HDS of DBT with the different catalysts

Catalyst	r_0 (mol/(L × h × g_{cat}))	k_1 (L/(s × g_{cat}))	HYD/DDS ratio[a]
NiW/Al_2O_3	2.0×10^{-2}	6.9×10^{-6}	0.4
NiW/SBA	4.1×10^{-2}	1.4×10^{-5}	0.7
NiW/Al-SBA	5.4×10^{-2}	1.9×10^{-5}	0.7
NiW/Ti-SBA	6.2×10^{-2}	2.2×10^{-5}	0.9
NiW/Zr-SBA	6.2×10^{-2}	2.2×10^{-5}	0.9

[a] Determined at 40% of total DBT conversion

HYD Hydrogenation pathway, *DDS* direct desulfurization pathway

HYD/DDS pathway ratio was determined as the ratio of HYD route main product (cyclohexylbenzene) to DDS route product (biphenyl)

necessary for the sulfur elimination via the perpendicular adsorption of the molecule through the S atom [1].

Conclusions

In this work, the synthesis of NiW-based HDS catalysts with a controlled dispersion of the oxide and sulfide phase was pursued by the use of both well-defined starting units (W precursor) and anchoring points on a high surface area support. A beneficial effect on the activity of HDS catalysts supported on modified SBA-15 materials is evident from the results presented above. Obtained results allow us to conclude the following:

Al-, Ti-, and Zr-containing SBA-15 type materials with relatively high Al_2O_3, TiO_2, and ZrO_2 loadings and without considerable degradation of the initial SBA-15 pore structure or long range periodicity order can be prepared by chemical grafting method. Chemical grafting resulted to be a suitable experimental technique leading to M-modified SBA supports with highly dispersed metal (Al, Ti, Zr) species.

All SBA-supported catalysts showed better performance in HDS of DBT than the conventional alumina-supported analog. When pure SBA-15 is used as support, its weak interaction with the W species leads to a heterogeneous distribution in the oxide precursor, which is reflected on the morphology of the active sulfide phase. All NiW/M-SBA catalysts showed a superior catalytic activity in HDS of DBT by enhancing the HYD route but Al-SBA support also promoted the cracking of the DBT molecule, which decreased liquid yield and product quality. Ti- and Zr-modified SBA-15 showed promising results as supports for NiW catalysts as they allow the formation of well dispersed and homogeneous W sulfides with an adequate morphology for the HDS of large molecules.

Acknowledgements Financial support by DGAPA-UNAM (grant IN-110609) is gratefully acknowledged. The authors thank M. Aguilar, I. Puente, and C. Salcedo for technical assistance.

References

1. Song C, Ma X (2003) Appl Catal B 41:207
2. Knudsen KG, Cooper BH, Topsøe H (1999) Appl Catal A 189:205
3. Song C (2003) Catal Today 86:211
4. Yoshimura Y, Toba M, Farag H, Sakanishi K (2004) Catal Surv Asia 8:47
5. Ito E, van Veen JAR (2006) Catal Today 116:446
6. Fujikawa T, Kimura H, Kiriyama K, Hagiwara K (2006) Catal Today 111:188
7. Gates BC, Topsøe H (1997) Polyhedron 16:3213
8. Spojakina A, Palcheva R, Jiratova K, Tyuliev G, Petrov L (2005) Catal Lett 104:45
9. Hensen EJM, van der Meer Y, van Veen JAR, Niemantsverdriet JW (2007) Appl Catal A 322:16
10. Kim CH, Yoon WL, Lee IC, Woo SI (1996) Appl Catal A 144:159
11. Breysse M, Cattenot M, Decamp T, Frety R, Gachet C, Lacroix M, Leclercq C, de Mourgues L, Portefaix JL, Vrinat M, Houari M, Grimbolt J, Kasztelan S, Bonelle JP, Housni S, Bachelier J, Duchet JC (1988) Catal Today 4:39
12. van der Vlies AJ, Prins R, Weber Th (2002) J Phys Chem B 106:9277
13. van der Meer Y, Hensen EJM, van Veen JAR, van der Kraan AM (2004) J Catal 228:433
14. Vissenberg MJ, van der Meer Y, Hensen EJM, de Beer BHJ, van der Kraan AM, van Santen RA, van Veen JAR (2001) J Catal 198:151
15. Chiranjeevi T, Kumar P, Maity SK, Rana MS, Murali Dhar G, Prasada Rao TSR (2001) Microporous Mesoporous Mater 44–45:547
16. Lizama L, Pérez M, Klimova T (2008) Stud Surf Sci Catal 174:1251
17. Hensen EJM, Kooyman PJ, van der Meer Y, van der Kraan AM, de Beer VHJ, van Veen JAR, van Santen RA (2001) J Catal 199:224
18. Klimova T, Calderón M, Ramírez J (2003) Appl Catal A 240:29
19. Klimova T, Lizama L, Amezcua JC, Roquero P, Terrés E, Navarrete J, Domínguez JM (2004) Catal Today 98:141
20. Amezcua JC, Lizama L, Salcedo C, Puente I, Domínguez JM, Klimova T (2005) Catal Today 107–108:578
21. Klimova T, Reyes J, Gutiérrez O, Lizama L (2008) Appl Catal A 335:159
22. Lizama L, Amezcua JC, Klimova T (2008) Stud Surf Sci Catal 174:1351
23. Gutiérrez OY, Fuentes GA, Salcedo C, Klimova T (2006) Catal Today 116:485

24. Muthu Kumaran G, Garg S, Soni K, Kumar M, Sharma LD, Murali Dhar G, Rama Rao KS (2006) Appl Catal A 305:123
25. Garg S, Soni K, Muthu Kumaran G, Kumar M, Gupta JK, Sharma LD, Murali Dhar G (2008) Catal Today 130:302
26. Zepeda T (2008) Appl Catal A 347:148
27. Zhao D, Huo Q, Feng J, Chmelka BF, Stucky GD (1998) J Am Chem Soc 120:6024
28. Zhao D, Feng J, Huo Q, Melosh N, Fredrickson GH, Chmelka BF, Stucky GD (1998) Science 279:548
29. Fenelonov VB, Romannikov VN, Derevyankin AY (1999) Microporous Mesoporous Mater 28:57
30. Cheng M, Wang Z, Sakurai K, Kumata F, Saito T, Komatsu T, Yashima T (1999) Chem Lett 2:131
31. Damyanova S, Dimitrov L, Mariscal R, Fierro JLG, Petrov L, Sobrados I (2003) Appl Catal A 256:183
32. Shenderovich IG, Buntkowsky G, Schreiber A, Gedat E, Sharif S, Albrecht J, Golubev NS, Findenegg GH, Limbach H (2003) J Phys Chem B 107:11924
33. Srinivasan S, Datye AK, Smith MH, Peden CHF (1994) J Catal 415:565
34. Laha SC, Mukherjee P, Sainkar SR, Kumar R (2002) J Catal 207:213
35. Alba MD, Luan Z, Klinowski J (1996) J Phys Chem B 100:2178
36. Smirnov KS, van de Graaf B (1996) Microporous Mater 7:133
37. Chaudhari K, Bal R, Das TK, Chandwadkar A, Srinivas D, Sivasanker S (2000) J Phys Chem B 104:11066
38. Zeng S, Blanchard J, Breysse M, Shi Y, Shu X, Nie H, Li D (2005) Microporous Mesoporous Mater 85:297
39. Gómez-Cazalilla M, Mérida-Robles JM, Gurbani A, Rodríguez-Castellón E, Jiménez-López A (2007) J Solid State Chem 180:1130
40. Davis RJ, Liu Z (1997) Chem Mater 9:2311
41. De Witte K, Busuioc AM, Meynen V, Mertens M, Bilba N, Van Tendeloo G, Cool P, Vansant EF (2008) Microporous Mesoporous Mater 110:100
42. Cozzolino M, Di Serio M, Tesser R, Santacesaria E (2007) Appl Catal A 325:256
43. Gao X, Wachs IE (1999) Catal Today 51:233
44. Infantes-Molina A, Mérida-Robles J, Maireles-Torres P, Finocchio E, Busca G, Rodríguez-Castellón E, Fierro JLG, Jiménez-López A (2004) Microporous Mesoporous Mater 75:23
45. Chen LF, Zhou XL, Noreña LE, Wang JA, Navarrete J, Salas P, Montoya A, Del Angel P, Llanos ME (2006) Appl Surf Sci 253:2443
46. Rodríguez-Castellón E, Jiménez-López A, Maireles-Torres P, Jones DJ, Rozière J, Trombetta M, Busca G, Lenarda M, Storaro L (2003) J Solid State Chem 175:159
47. Ko JB, Lee SW, Kim DE, Kim YU, Li G, Lee SG, Chang TS, Kim D, Joo YL (2006) J Porous Mater 13:325
48. Klein S, Weckhuysen BM, Martens JA, Maier WF, Jacobs PA (1996) J Catal 163:489
49. Gao X, Fierro JLG, Wachs IE (1999) Langmuir 15:3169
50. Luan Z, Maes EM, van der Heide PAW, Zhao D, Czernuszewicz RS, Kevan L (1999) Chem Mater 11:3680
51. Peña ML, Dellarocca V, Rey F, Corma A, Coluccia S, Marchese L (2001) Microporous Mesoporous Mater 44–45:345
52. Newalkar BL, Olanrewaju J, Komarneni S (2001) Chem Mater 13:552
53. Rakshe B, Ramaswamy V, Hegde SG, Vetrivel R, Ramaswamy AV (1997) Catal Lett 45:41
54. Ciuparu D, Ensuque A, Shafeev G, Bozon-Verduaz F (2000) J Mater Sci Lett 19:931
55. Benitez VM, Figoli NS (2002) Catal Commun 3:487
56. Vermaire DC, Van Berge PC (1989) J Catal 116:309
57. Logie V, Maire G, Michel D, Vignes JL (1999) J Catal 188:90
58. Chen XR, Chen CL, Xu NP, Mou CY (2004) Catal Today 93–95:129
59. Yang XL, Dai WL, Gao R, Fan K (2007) J Catal 249:278
60. Hodnett BK, Moffat JB (1985) J Catal 91:93
61. Palcheva R, Spojakina A, Tyuliev G, Jiratova K, Petrov L (2007) Kinet Catal 48:847
62. Tuel A (1999) Microporous Mesoporous Mater 27:151
63. Girgis MJ, Gates BC (1991) Ind Eng Chem Res 30:2021
64. Houalla M, Nag NK, Sapre AV, Broderick DH, Gates BC (1978) AIChE J 24:1015